Mechanosensitive remodeling of the bacterial flagellar motor is independent of direction of rotation

Navish Wadhwa[a,b,1], Yuhai Tu[c], and Howard C. Berg[a,b]

[a]Department of Molecular and Cellular Biology, Harvard University, Cambridge, MA 02138; [b]Rowland Institute at Harvard, Harvard University, Cambridge, MA 02142; and [c]T. J. Watson Research Center, IBM, Yorktown Heights, NY 10598

Motility is important for the survival and dispersal of many bacteria, and it often plays a role during infections. Regulation of bacterial motility by chemical stimuli is well studied, but recent work has added a new dimension to the problem of motility control. The bidirectional flagellar motor of the bacterium *Escherichia coli* recruits or releases torque-generating units (stator units) in response to changes in load. Here, we show that this mechanosensitive remodeling of the flagellar motor is independent of direction of rotation. Remodeling rate constants in clockwise rotating motors and in counterclockwise rotating motors, measured previously, fall on the same curve if plotted against torque. Increased torque decreases the off rate of stator units from the motor, thereby increasing the number of active stator units at steady state. A simple mathematical model based on observed dynamics provides quantitative insight into the underlying molecular interactions. The torque-dependent remodeling mechanism represents a robust strategy to quickly regulate output (torque) in response to changes in demand (load).

bacterial motility | flagellar motor | self-assembly | molecular motors | *Escherichia coli*

Many bacteria swim through aqueous environments to acquire resources, to disperse progeny, and to infect hosts (1, 2). The rotation of flagella (3, 4), powered by the bidirectional flagellar motor (5–7), drives motility in many bacteria. In *Escherichia coli*, the flagellar motor consists of over 20 different proteins that self-assemble at the cell wall in varying copy numbers (8–10). Motor structure (Fig. 1*A*) includes a rotor embedded in the inner cell membrane, a drive shaft, and a flexible hook that transmits torque to the filament (10, 11). The cytoplasmic ring (C ring), which contains copies of the proteins FliG, FliM, and FliN, is mounted on the cytoplasmic face of the rotor and is responsible for directional switching of the motor (12). The rotor is driven by up to 11 ion-powered $MotA_5B_2$ stator units (13–16) that surround the rotor and generate torque. MotA engages FliG, whereas MotB is mounted on the rigid framework of the peptidoglycan cell wall (17–20). Motor-bound units exchange with a pool of unbound units in the inner membrane (10, 21).

Motor function is regulated by inputs from the environment. Detection of specific ligands by chemoreceptors drives a two-component signaling cascade that controls the direction of rotation of the motor (22–24). Upon binding the response regulator CheY-P, the C ring undergoes a concerted conformational change that reverses motor rotation from counterclockwise (CCW) to clockwise (CW), as viewed from outside the cell. This change in the direction of rotation is the basis of run-and-tumble motility in *E. coli* (CCW = run, CW = tumble). Changes in viscous load trigger remodeling of the stator (25–27), whereby, at high loads, the number of motor-bound stator units increases, and vice versa. Dynamics of stator remodeling have only been quantified in CCW rotating motors, using electrorotation (28) and magnetic tweezers (29, 30). The observed dynamics were rationalized using the CCW torque–speed (T-S) relationship (Fig. 1*B*) (28). CCW and CW rotating motors have different T-S

relationships (Fig. 1*B*), likely due to differences in stator–rotor interactions (31–33). How the differences in T-S relationship affect stator remodeling in CW motors is unknown. Additionally, the molecular mechanisms underlying the load-dependent remodeling phenomenon remain poorly understood.

Here, we use electrorotation to study the dynamics of load-dependent stator remodeling in CW rotating motors. We find that, just like CCW motors, CW rotating flagellar motors release their stator units when the motor torque is low, and recruit stator units when the torque increases again. The rates of stator unit release and recruitment in CW and CCW motors collapse onto a single curve when plotted against torque, despite their dissimilar T-S relationships. The collapse of remodeling data suggests a universal model for torque dependence in the mechanically regulated remodeling of the bacterial flagellar motor. Our in vivo measurements of stator assembly dynamics advance the understanding of a large protein complex with multiple parts.

Results

CCW motors have a unique T-S relationship among rotary molecular motors; the torque exerted by CCW motors remains nearly constant at low speeds up to a so-called "knee-speed," beyond which it rapidly drops to zero (Fig. 1*B*). In contrast, torque produced by CW rotating motors drops linearly from stall to zero (31). In addition, the CW mutant strain used here has a significantly smaller stall torque and zero-torque speed than that of the CCW mutant strain used for comparison (Fig. 1*B*; also see *Materials and Methods*). These differences allow us to tease apart the roles of motor torque and speed in load-dependent stator remodeling.

Significance

Macromolecular machines carry out most of the biological functions in living organisms. Despite their significance, we do not yet understand the rules that govern the self-assembly of large multiprotein complexes. The bacterial flagellar motor tunes the assembly of its torque-generating stator complex with changes in external load. Here, we report that clockwise and counterclockwise rotating motors have identical remodeling responses to changes in the external load, suggesting a purely mechanical mechanism for this regulation. Autonomous control of self-assembly may be a general strategy for tuning the functional output of protein complexes. The flagellar motor is a prime example of a macromolecular machine in which the functional regulation of assembly can be rigorously studied.
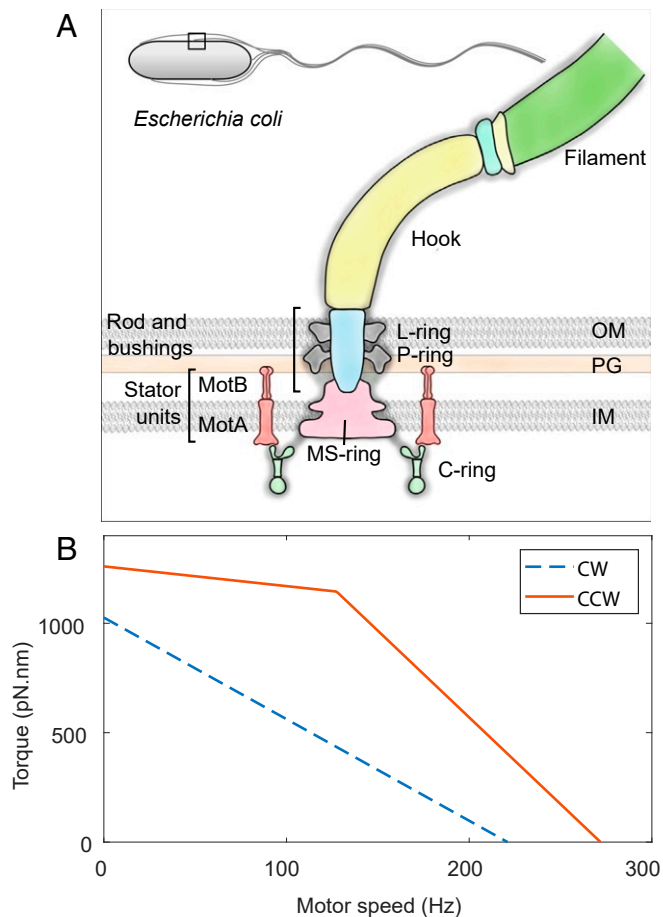

Fig. 1. Bacterial flagellar motor's structure and its T-S curve. (*A*) Schematic representation of the flagellar motor of Gram-negative bacteria. The rotor consists of the MS ring (M for membranous and S for supramembranous) embedded in the inner membrane (IM) and the C ring embedded in the cytoplasm. Stator units (MotA–MotB complexes) that span the inner membrane bind to the peptidoglycan (PG) layer and apply torque on the C ring. The torque is transmitted via a rod (driveshaft) and a flexible hook (universal joint) to the flagellar filament. L and P rings (L for lipopolysaccharide and P for peptidoglycan) are embedded in the outer membrane (OM) and the peptidoglycan, respectively, and act as bushings. *Inset* shows the outline of an *E. coli* cell with a square demarcating the region that is represented in detail. (*B*) T-S curve of the CCW (solid orange) and CW (dashed blue) rotating flagellar motors compared in this study. Data are from refs. 31 and 58. See *Materials and Methods* for details.

We tethered bacterial cells to the surface of a sapphire window via short filament stubs (Fig. 2*A*). With the filament immobilized, the motor rotated the cell body at a low speed and operated close to stall. We observed motor output in this manner for 30 s. Then we turned the electrorotation field ON, which applied an assisting external torque on the cell (see *Materials and Methods*), thereby decreasing the load on the motor. As a result, the cell rotation sped up, and the motor torque decreased. To observe any changes in the number of active stator units, we turned electrorotation OFF for 1 s every 9 s, when the motor rotation due solely to the bound stator units could be measured. We repeated this cycle of 8 s ON followed by 1 s OFF for 10 min, after which we kept electrorotation OFF. Removal of electrorotation field removed the assisting torque and increased the load on the motor. The speed of the motor was now measured continuously. We observed the motor rotation in this manner for an additional 10 min.

When we decreased motor load by driving a tethered cell forward with electrorotation, the motor's native speed (measured during the OFF intervals) decreased, indicating a loss of stator units driving the motor. Fig. 2*B* shows the results of a typical experiment, in which the electrorotation speed during the ON intervals was fixed at 200 Hz. Starting at ~14 Hz before electrorotation, this motor's speed decreased in a stepwise manner to 0 Hz during the electrorotation period, indicating a complete loss of the bound stator units. The removal of electrorotation field after 10 min promoted the recruitment of stator units, indicated by a stepwise increase in the motor speed. We fitted steps to the speed data, from which we estimated the unitary step height corresponding to the gain or loss of single stator units. By dividing the speed levels by the unitary step height, we calculated the number of bound stator units as a function of time (Fig. 2*C*).

We conducted these experiments at five electrorotation speeds, ranging from 50 Hz to 250 Hz. These speeds cover the entire range of torque generation by the CW rotating motors, which decreases linearly from stall torque at 0 Hz to zero torque at 221 Hz (Fig. 1*B*). The dynamics of stator remodeling depended strongly on the electrorotation speed. We observed no remodeling for electrorotation at 50 Hz within the duration of the experiment (Fig. 3*A*). For the other electrorotation
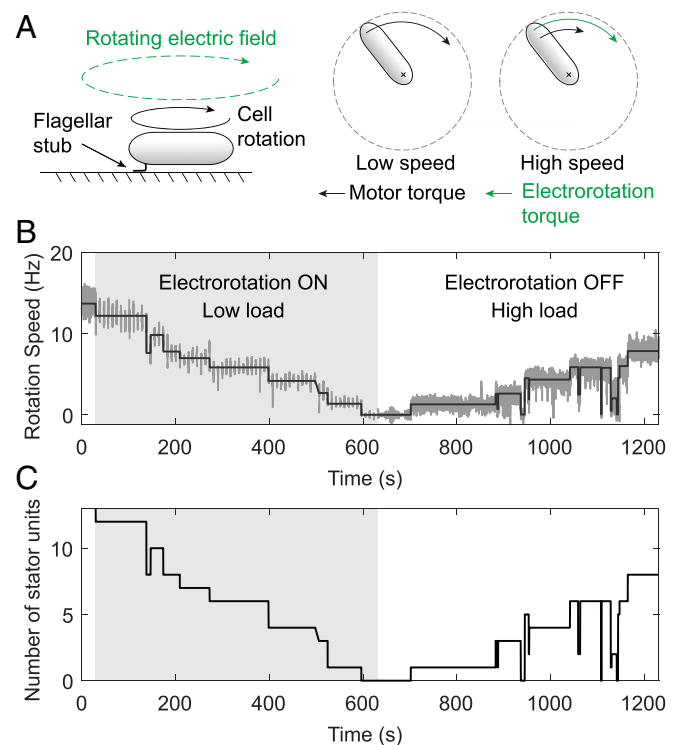

Fig. 2. Control of motor load using electrorotation. (*A*) The cell is tethered to a surface via a short flagellar stub (*Left*). The motor exerts a large torque to rotate the cell body, depicted by the black arrow (*Middle*). A high-frequency rotating electric field applies an external torque (green) on the cell. The external torque spins the cell at high speed and reduces the motor torque (*Right*). Also see *Materials and Methods*. (*B*) Example of an experimental output showing motor speed (dark gray) as a function of time for an electrorotation speed of 200 Hz. At the start of the experiment, motor speed was measured continuously for 30 s without any stimuli, after which electrorotation was turned ON, depicted by the light gray region. During electrorotation, motor speed was measured for 1 s every 9 s. After 10 min of electrorotation, the field was turned OFF, increasing the load on the motor. Solid black line represents steps fitted on the speed data. (*C*) Number of active stator units vs. time for the same data.
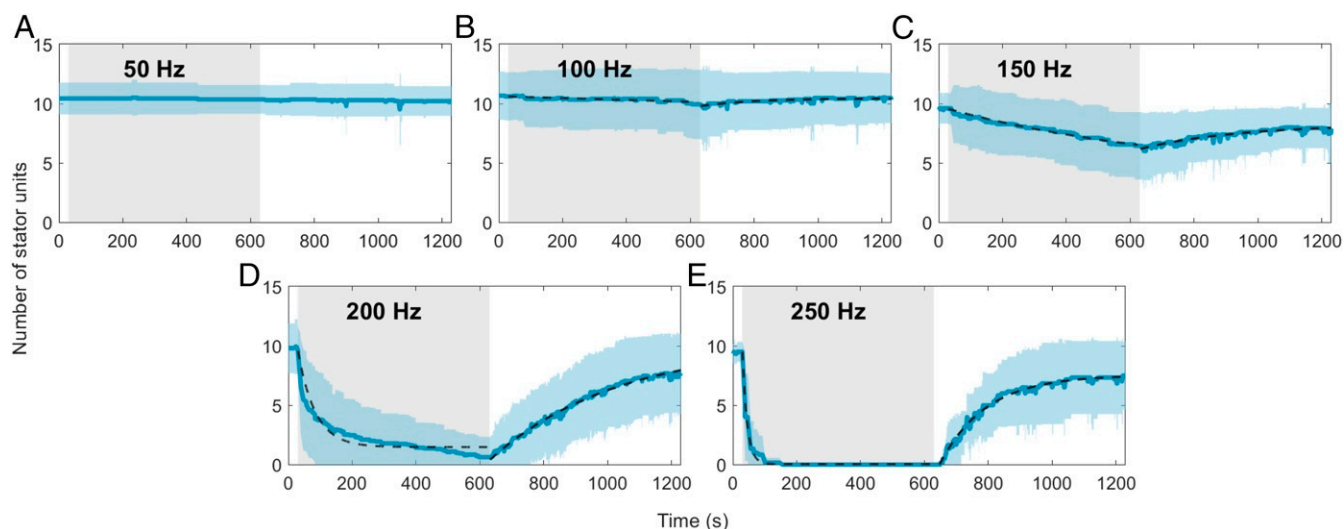
Fig. 3. Number of stator units vs. time for different CW electrorotation speeds: (*A*) 50, (*B*) 100, (*C*) 150, (*D*) 200, and (*E*) 250 Hz. The solid blue line is the average for a given electrorotation speed, and the shaded blue region represents the SD. Fits of Hill–Langmuir model (Eq. **2**) on the data are depicted as dashed lines, except in *A* (electrorotation at 50 Hz), in which no remodeling was observed. The shaded gray region represents the electrorotation period. Sample sizes for *A*–*E* are 14, 15, 18, 19, and 6, respectively.

speeds, we observed a clear response to the reduction in load. Higher electrorotation speeds resulted in a bigger loss of stator units and at a greater rate (Fig. 3 *B–E*). In all cases, the loss of the stator units during the electrorotation period was followed by a period of recovery after electrorotation was switched OFF.

The population-averaged kinetics of the stator remodeling process can be described by the Hill–Langmuir model as adopted by Nord et al. (29). An unbound stator unit can occupy one of the available sites on the periphery of the rotor with N binding sites. We fitted this model to the measured dynamics (Fig. 3), obtaining the population-averaged on rate k_+ and the off rate k_- for the interaction between a single stator unit and the motor. Most of the variation between experimental conditions was contained in k_- (Fig. 4*A*). In contrast, k_+ measured during the electrorotation period showed little variation across experimental conditions (Fig. 4*B*); k_+ was, however, higher during the recovery period in which the torque was high. We compared these rates with the data we obtained for CCW rotating motors (28). Interestingly, the two sets of data collapse if plotted against the torque per stator unit Γ (Fig. 4*A*). This is striking because CW and CCW rotating motors produce different torques at any given speed (Fig. 1*B*) and have different remodeling kinetics at a given electrorotation speed. The collapse of the two datasets despite these differences demonstrates that torque is the main parameter governing load-dependent stator remodeling. No collapse was seen when the data were plotted against the motor rotation speed (Fig. 4 *A, Inset* and *B, Inset*).

The difference between the effective free energy of bound and unbound stator units (ΔF) can be defined from a logarithm of the ratio of the forward and backward rates ($\Delta F = k_B T \log k_-/k_+$), and determines whether the binding is favorable (Fig. 5*A*). Plotted against torque per stator unit (Γ), the values of ΔF measured for CW and CCW motors also collapsed onto a single curve, which exhibits a linear decrease in ΔF with Γ. The slope of a linear fit was given by $\lambda = 0.047 \ k_B T \cdot \mathrm{pN}^{-1} \cdot \mathrm{nm}^{-1}$. But note that λ is a dimensionless quantity (energy and torque have the same units), giving $\lambda = 0.19$ in dimensionless units. The intercept of the linear fit was positive at $\Delta F_0 \approx 3.2 \ k_B T$, indicating that

at zero torque, the binding of stator units to the motor is unfavorable. A model of k_- based on the linear fit of ΔF against Γ captured the observed dependence of k_- on torque (Fig. 4*A*).

Discussion

Our results show not only that load-dependent stator remodeling takes place in flagellar motors rotating in either direction but that the remodeling dynamics as a function of motor torque are identical in CW and CCW rotating motors. A reduction in load triggers a decline in the number of active stator units in both CW and CCW rotating motors, whereas an increase in load promotes an increase in the number of stator units (Fig. 3). In both CCW and CW rotating motors, the kinetics of stator remodeling are determined by the torque exerted by the stator units (Fig. 4). As noted before (29), torque-dependent remodeling in the flagellar motor provides a specific example of how a catch bond (one where binding becomes stronger with tension) can lead to fast mechano-adaptation (34, 35).

The effective free energy difference between bound and unbound units at zero torque (ΔF_0) is positive, suggesting that the binding of stator units is energetically unfavorable. Thus, the production of torque from the motor is required for driving stator assembly. The range of ΔF measured here, from around $-4 \ k_B T$ to $6 \ k_B T$, is comparable to the energy available from proton motive force (PMF) per proton in a fully energized cell ($\sim 6 \ k_B T$) (36). As torque is proportional to PMF for a given load (36), a lower PMF would restrict the motor to a narrower range of ΔF (Fig. 5*B*) without affecting the slope of the $\Delta F - \Gamma$ relationship. Lower torque resulting from a lower PMF would increase k_- (Fig. 4*A*) without affecting k_+ in most cases (Fig. 4*B*), consistent with recent observations in cells affected by the ionophore butanol (30).

The values of the model parameters provide quantitative insight into the physiochemical interactions underlying stator remodeling. The off rate k_- is the same between the CCW and CW conformations, suggesting that it depends only on the stator–peptidoglycan interactions, which, in turn, depend on torque but not on the exact mechanisms of torque generation. An increase in the torque exerted by a bound stator unit lowers its effective free energy (Fig. 5*B*). Torque (Γ) is equal to the radius of the
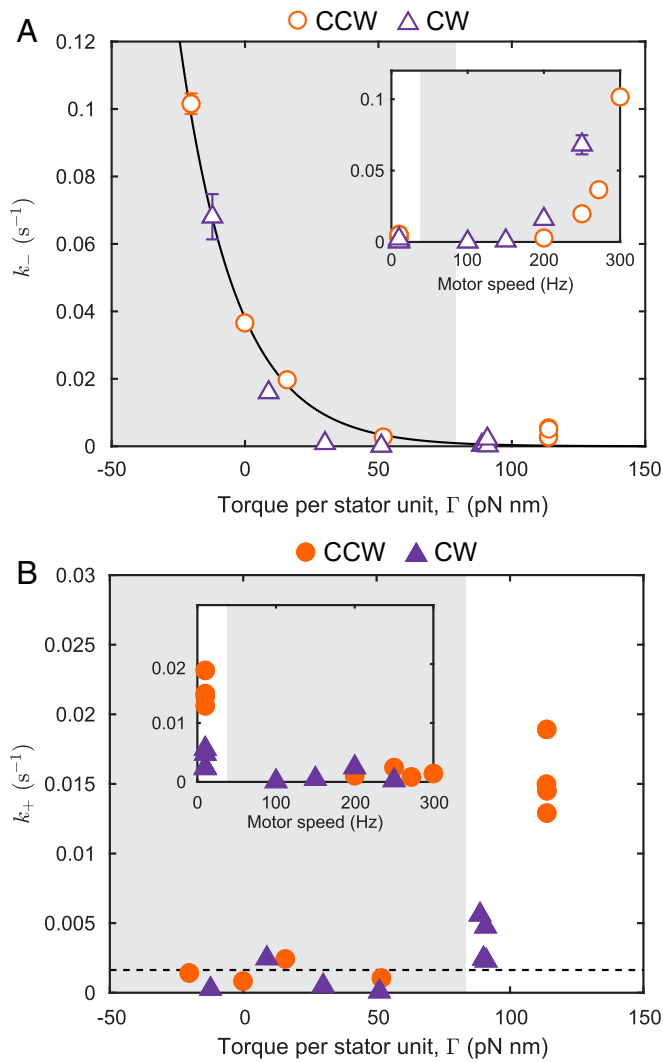
Fig. 4. Data collapse if plotted against torque. (*A*) The off rate k_- (open symbols) as a function of torque per stator unit Γ, for CW (purple triangles) and CCW (orange disks) rotating motors. The solid line is the model $k_- = k_+ e^{(\Delta F_0 - \lambda \Gamma)/k_B T}$, with $k_+ = 0.0016$ s^{-1}, $\Delta F_0 = 3.2\, k_B T$, and $\lambda = 0.047$ $k_B T.$pN$^{-1}.$nm^{-1}, where k_B and T are the Boltzmann constant and the absolute temperature, respectively. *Inset* shows the same data plotted against motor rotation speed. (*B*) The on rate k_+ (solid symbols) as a function of Γ, for CW (purple triangles) and CCW (orange disks) rotating motors. The dashed line is $k_+ = 0.0016$ s^{-1}. *Inset* shows the same data plotted against motor rotation speed.

step process. In unbound stator units, the proton channels are blocked by a plug that is a part of the periplasmic domain of MotB (37, 38). Somehow, when an unbound stator unit collides with the rotor, the plug opens, unblocking the proton channel to allow torque generation, and the stator unit binds the peptidoglycan (19, 39). First, the interaction between the FliG and MotA drives conformational changes in the stator unit that unplug the channel and extend the periplasmic domain of MotB to the peptidoglycan layer (40, 41). Second, the periplasmic domain binds to the peptidoglycan layer and anchors the stator unit. The first step could be hindered by the rotation of the C ring, which might impair the interaction between MotA and individual FliG subunits. This could explain the higher on rate during the recovery period, in which the torque is large and motor rotation speed is small. The reason for the independence of k_+ from torque
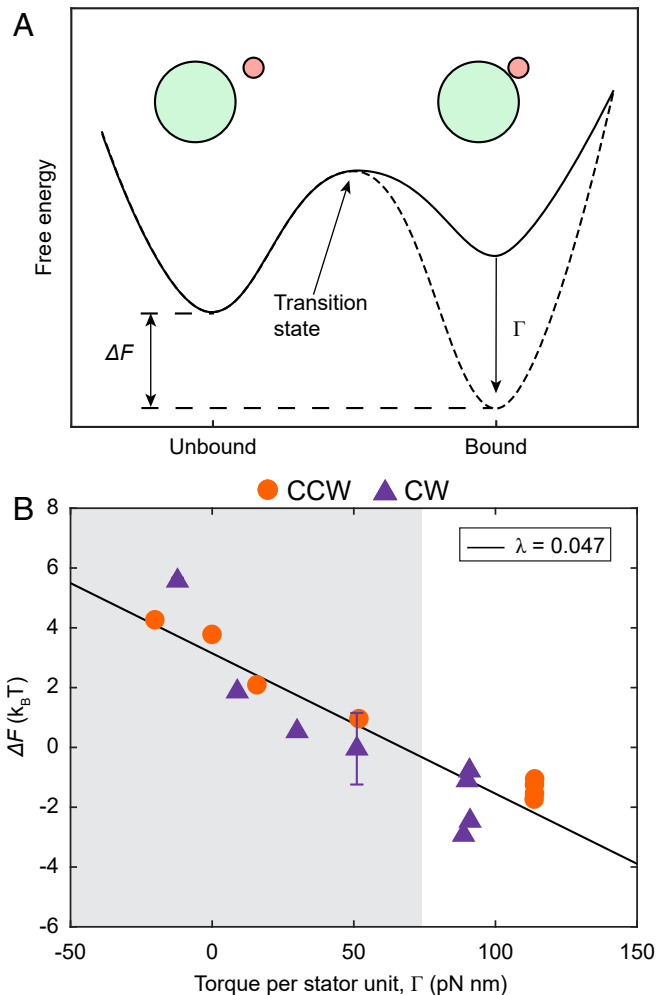

Fig. 5. Torque tunes the effective free energy profile of stator binding. (*A*) Schematic representation of how increased torque promotes stator assembly. At low torque (solid curve), the free energy of the bound stator units is greater than that of unbound units, making assembly unfavorable. Increase in torque reduces the free energy of bound units (dashed curve), making assembly favorable. ΔF is the difference between the free energy of bound and unbound units. Green and pink circles represent the C ring and the stator unit, respectively. (*B*) ΔF as a function of torque per stator unit Γ, for CW (purple triangles) and CCW (orange disks) rotating motors. The solid black line is linear fit to the data, and has a slope $\lambda = 0.047$ $k_B T.$pN$^{-1}.$nm^{-1} or 0.19 in dimensionless units. The shaded and blank regions indicate data obtained from the electrorotation and the recovery periods, respectively. Error bars are 1 SE in each direction.

C ring [$R \approx 22.5$ nm (5)], multiplied by the tangential force (f) applied by MotA on FliG, that is, $\Gamma = fR$. Thus, the linear fit in Fig. 5*B* with slope $\lambda = 0.19$ leads to $\Delta F = \Delta F_0 - \lambda\Gamma = \Delta F_0 - fl$, where $\Delta F_0 \approx 3.2 k_B T$, and l is a length scale $l = \lambda R \approx 4$ nm. Assuming the transitions between the bound and unbound state of the stator go through a transition state (Fig. 5*A*), this length scale denotes the average displacement of the bound state from the transition state along the direction of the force between FliG and MotA, accompanied by a decrease in the free energy equal to the force times the displacement. It is interesting to note that a displacement of 4 nm is within the relevant size range, given that a stator unit is 9 nm high and 7.5 nm wide (15). It is possible that 4 nm represents either an upper limit or a preferred state for the deformation of MotB peptidoglycan binding (PGB) domain.

According to current (incomplete) understanding, the on rate k_+ of a stator to the motor is controlled by a complex multi-

for the low to intermediate torque range (Fig. 4B) remains unclear.

Cryoelectron microscopy structures of stator units were obtained recently and provide additional insights into stator function and assembly (15, 16). The structures suggest that CW rotation of the MotA pentamer around the MotB dimer drives rotation of the C ring. During CCW rotation, the C ring adopts a narrow conformation, and stator units interact with the outside of the ring (32, 42). Upon binding the chemotaxis response regulator CheY-P, the C ring expands, and the stator units now interact with the inside of the C ring, driving CW rotation (32, 42). These structural changes in the C ring are the likely source of the asymmetry in the T-S relationship of CCW and CW rotating flagellar motors (31, 33). Yet, at the location where MotB binds peptidoglycan, CW and CCW rotation should be indistinguishable, because neither the peptidoglycan nor MotB is known to have any CW–CCW asymmetry. This symmetry in the MotB–peptidoglycan interaction is likely responsible for the CW–CCW symmetry in torque dependence of k_-. In CW rotating motors, an unbound stator unit must not only collide with the rotor but also reach the inside of the C ring before it can bind the motor. Therefore, the binding of stator units in CW rotating motors is less likely than in CCW rotating motors, consistent with the lower k_+ in CW motors during the recovery period.

Crystal structure of the PGB domain of MotB is known (19). However, the structure provides only limited insight into stator stabilization, since it does not reveal the load-dependent deformations in either the MotB PGB domain or the peptidoglycan. Importantly, neither crystal structures nor cryotomograms provide information on dynamics. We have shown here and in previous work (28) that motor remodeling depends on dynamic aspects of the stator assembly that are determined by the binding and unbinding of the stator units to the motor. Therefore, a comprehensive understanding of this process requires knowledge of dynamics in addition to the structure. Our work provides this information in quantitative detail.

The biological function of stator remodeling is not fully understood, but both sensory and regulatory roles are possible (10). Load-dependent remodeling of stator units acts like regulated cylinder deactivation in car engines, increasing power output when the demand is high and decreasing output when the demand is low, which serves as a mechanism to save energy. Another likely role of stator remodeling is that of mechanosensitive signaling, in particular, during interaction with surfaces (43–47). Increasing evidence supports the idea that proximity to surfaces increases the load on the motor, which is signaled to downstream processes via a cascade that starts with motor remodeling (48–53). In this manner, stator remodeling might play an important ecological role for bacteria, particularly during the initial stages of biofilm formation.

How cells control the assembly and function of large macromolecular complexes remains a fundamental problem in biology (54–56). It often involves gene regulation, in which a signal of interest triggers a change in the transcription or the translation of genes encoding the assembly components. This process takes at least several minutes and is therefore ill suited for fast-changing environmental signals. The alternative approach, employed by the bacterial flagellar motor, involves direct control of the assembly by the signal of interest. The latter strategy has the advantage that the assembly/disassembly can be triggered directly, allowing the cell to quickly respond and adapt to sudden changes in mechanical cues.

Materials and Methods

Bacterial Strains and Cultures. The strain used in this study (HCB1797; JY32+pWB5+pKF131) was constructed by Junhua Yuan and is previously described (31). Briefly, an in-frame deletion of *fliC* in VS149 [Δ(*cheR-cheZ*)] yielded JY32, which was transformed with two compatible plasmids: pWB5 (AmpR) expressing wild-type *cheY* under an Isopropyl β-D-1-thiogalactopyranoside (IPTG)-inducible promotor, and pKAF131 (CamR) expressing sticky *fliC* under the native promoter of *fliC*. Cells were grown at 33 °C in 10 mL of tryptone broth containing 100 μg/mL ampicillin, 25 μg/mL chloramphenicol, and 0.1 mM IPTG to OD_{600} between 0.5 and 0.7. Cells were harvested by centrifuging at 1,200 × *g* for 7 min and resuspended in 1 mL of electrorotation buffer [20 mM N-[Tris(hydroxymethyl)methyl]-2-aminoethanesulfonic acid (TES), 0.1 mM ethylenediaminetetraacetic acid (EDTA), pH 7.5]. Flagellar filaments were sheared off by passing the cell suspension through a piece of polyethylene tubing (20 cm long, inner diameter 0.58 mm) 60 times. The cells were pelleted again and resuspended in 5 mL of buffer.

Electrorotation Apparatus and Data Acquisition. The electrorotation apparatus was as described before (28, 57). Briefly, the cells were tethered to a sapphire window in a custom-built flow cell that included the tips of four tungsten microelectrodes a short distance from the surface. Sapphire was used for its high thermal conductivity. The electrodes were driven in quadrature using custom-built electronics. This applied a tunable external torque on the cells tethered on the sapphire surface. The temperature of the sapphire window was sensed by a small thermistor and held at 20 °C by a circular Peltier element driven by a proportional controller. The flow cell together with the electrode assembly was fixed to a 20× objective of a phase contrast microscope. The light diffracted from the cell was split into two parts; one was imaged onto a high-speed scientific Complementary metal–oxide–semiconductor (sCMOS) camera and the other onto a pair of photomultipliers via a linear-graded filter setup (57). The photomultiplier signal was used for live measurement of the motor speed (same as the rotation speed of the cell body) during the experiment, and the sCMOS images were used for offline analysis using custom-written MATLAB scripts.

Data Analysis. The data analysis procedure was as described before (28). Angular displacement of the cell between frames was multiplied by the frame rate to obtain the rotation speed, which was filtered by a median filter of order 15. The rotation speed was fitted with steps using a custom algorithm described before (25, 28). The distribution of fitted step heights had two peaks—the first dominant peak due to the addition of a single stator unit, and the second smaller peak due to the addition of two units within a short time interval. We used the unitary step height obtained from the first peak for estimating the number of active stator units from the speed traces.

T-S Curve for HCB1797 at 20 °C. The CW T-S curve lacks the characteristic "knee" of the CCW T-S curve, and torque decreases linearly from stall to the zero torque (31). Additionally, the stall torque and the zero-torque speeds of HCB1797 (a derivative of RP437) are smaller than those of the strain HCB986 (a derivative of AW405) that was used in the experiments on CCW rotating motors. The numerical factor for scaling the torque and speed from AW405 to RP437 is 285/350 (31). We therefore derived the T-S curve for HCB1797 by scaling down the stall torque and zero-torque speeds for HCB986 [1,260 pN nm and 272 Hz, respectively (28, 58)] and linearly interpolating between those points.

Hill–Langmuir Model for Stator Assembly. The population-averaged kinetics of changes in the number of stator units bound to the motor can be represented by the differential equation

$$\frac{d\langle n \rangle}{dt} = k_+(N - \langle n \rangle) - k_- \langle n \rangle, \qquad [1]$$

where $\langle n \rangle$ is the ensemble averaged number of stator units bound to the motor at time t, k_+ and k_- are the population-averaged on rate and the off rate for the binding of a single stator unit to the motor, and N is the number of binding sites, assumed to be 11 (14). The time-dependent solution for an initial condition $\langle n \rangle(0) = n_0$ is

$$\langle n \rangle(t) = \langle n \rangle_{ss} + (n_0 - \langle n \rangle_{ss})e^{-\frac{t}{\tau}}, \qquad [2]$$

where $\langle n \rangle_{ss} = Nk_+/k_+ + k_-$ is the steady-state number of stator units, and $\tau = 1/k_- + k_+$ is the time constant for the exponential approach to steady state. We fitted Eq. **2** to the experimentally determined number of stator units, obtaining $\langle n \rangle_{ss}$ and τ. Each experimental condition required two separate fits—one for the dissociation of stator units during electrorotation and another for their assembly after electrorotation was switched OFF (Fig. 3).

Wadhwa et al.
Mechanosensitive remodeling of the bacterial flagellar motor is independent of direction of rotation

PNAS | 5 of 6
https://doi.org/10.1073/pnas.2024608118

From each pair of $\langle n \rangle_{ss}$ and τ, we calculated k_+ and k_- for the given value of torque per stator unit Γ specified by the T-S curve.

Model for Torque Dependence. We developed a model for including torque dependence in the dynamics of stator assembly (28). We assume that, at zero torque, the binding of a single stator unit to the motor decreases its free energy by an amount ΔF_0. An increase in motor toque decreases the free energy of a bound stator unit further by an amount ϵ_T that depends on torque. Thus, the effective free energy difference between the bound and unbound states of a stator unit at a given torque is $\Delta F = \Delta F_0 - \epsilon_T$, where the torque dependence is fully contained in ϵ_T. From equilibrium statistical mechanics, we can get ΔF in terms of k_- and k_+ as $\Delta F = k_B T \log k_- / k_+$, where k_B and T are the Boltzmann constant and the absolute temperature,

respectively. We fitted a linear model on the measured value of ΔF, given by $\Delta F = \Delta F_0 - \lambda \Gamma$, where λ is the constant of proportionality. A linear fit on ΔF against Γ gave the intercept ΔF_0 as well as the slope λ. Assuming that k_+ remains constant, k_- could be modeled from the linear fit on ΔF as $k_- = k_+ e^{\Delta F / k_B T} = k_+ e^{(\Delta F_0 - \lambda \Gamma)/k_B T}$.

1. C. Josenhans, S. Suerbaum, The role of motility as a virulence factor in bacteria. *Int. J. Med. Microbiol.* **291**, 605–614 (2002).
2. B. Chaban, H. V. Hughes, M. Beeby, The flagellum in bacterial pathogens: For motility and a whole lot more. *Semin. Cell Dev. Biol.* **46**, 91–103 (2015).
3. H. C. Berg, R. A. Anderson, Bacteria swim by rotating their flagellar filaments. *Nature* **245**, 380–382 (1973).
4. M. Silverman, M. Simon, Flagellar rotation and the mechanism of bacterial motility. *Nature* **249**, 73–74 (1974).
5. H. C. Berg, The rotary motor of bacterial flagella. *Annu. Rev. Biochem.* **72**, 19–54 (2003).
6. Y. Sowa, R. M. Berry, Bacterial flagellar motor. *Q. Rev. Biophys.* **41**, 103–132 (2008).
7. S. Chen et al., Structural diversity of bacterial flagellar motors. *EMBO J.* **30**, 2972–2981 (2011).
8. F. F. V. Chevance, K. T. Hughes, Coordinating assembly of a bacterial macromolecular machine. *Nat. Rev. Microbiol.* **6**, 455–465 (2008).
9. L. D. B. Evans, C. Hughes, G. M. Fraser, Building a flagellum outside the bacterial cell. *Trends Microbiol.* **22**, 566–572 (2014).
10. J. P. Armitage, R. M. Berry, Assembly and dynamics of the bacterial flagellum. *Annu. Rev. Microbiol.* **74**, 181–200 (2020).
11. S. Nakamura, T. Minamino, Flagella-driven motility of bacteria. *Biomolecules* **9**, 279 (2019).
12. T. Minamino, M. Kinoshita, K. Namba, Directional switching mechanism of the bacterial flagellar motor. *Comput. Struct. Biotechnol. J.* **17**, 1075–1081 (2019).
13. S. Khan, M. Dapice, T. S. Reese, Effects of mot gene expression on the structure of the flagellar motor. *J. Mol. Biol.* **202**, 575–584 (1988).
14. S. W. Reid et al., The maximum number of torque-generating units in the flagellar motor of Escherichia coli is at least 11. *Proc. Natl. Acad. Sci. U.S.A.* **103**, 8066–8071 (2006).
15. M. Santiveri et al., Structure and function of stator units of the bacterial flagellar motor. *Cell* **183**, 244–257 (2020).
16. J. C. Deme et al., Structures of the stator complex that drives rotation of the bacterial flagellum. *Nat. Microbiol.* **5**, 1553–1564 (2020).
17. J. Zhou, S. A. Lloyd, D. F. Blair, Electrostatic interactions between rotor and stator in the bacterial flagellar motor. *Proc. Natl. Acad. Sci. U.S.A.* **95**, 6436–6441 (1998).
18. S. Kojima, D. F. Blair, Solubilization and purification of the MotA/MotB complex of Escherichia coli. *Biochemistry* **43**, 26–34 (2004).
19. S. Kojima et al., Stator assembly and activation mechanism of the flagellar motor by the periplasmic region of MotB. *Mol. Microbiol.* **73**, 710–718 (2009).
20. Y. Chang et al., Structural insights into flagellar stator–rotor interactions. *eLife* **8**, e48979 (2019).
21. M. C. Leake et al., Stoichiometry and turnover in single, functioning membrane protein complexes. *Nature* **443**, 355–358 (2006).
22. G. H. Wadhams, J. P. Armitage, Making sense of it all: Bacterial chemotaxis. *Nat. Rev. Mol. Cell Biol.* **5**, 1024–1037 (2004).
23. J. S. Parkinson, G. L. Hazelbauer, J. J. Falke, Signaling and sensory adaptation in Escherichia coli chemoreceptors: 2015 update. *Trends Microbiol.* **23**, 257–266 (2015).
24. S. Bi, V. Sourjik, Stimulus sensing and signal processing in bacterial chemotaxis. *Curr. Opin. Microbiol.* **45**, 22–29 (2018).
25. P. P. Lele, B. G. Hosu, H. C. Berg, Dynamics of mechanosensing in the bacterial flagellar motor. *Proc. Natl. Acad. Sci. U.S.A.* **110**, 11839–11844 (2013).
26. M. J. Tipping, N. J. Delalez, R. Lim, R. M. Berry, J. P. Armitage, Load-dependent assembly of the bacterial flagellar motor. *mBio* **4**, e00551 (2013).
27. R. Chawla, K. M. Ford, P. P. Lele, Torque, but not FliL, regulates mechanosensitive flagellar motor-function. *Sci. Rep.* **7**, 5565 (2017).
28. N. Wadhwa, R. Phillips, H. C. Berg, Torque-dependent remodeling of the bacterial flagellar motor. *Proc. Natl. Acad. Sci. U.S.A.* **116**, 11764–11769 (2019).
29. A. L. Nord et al., Catch bond drives stator mechanosensitivity in the bacterial flagellar motor. *Proc. Natl. Acad. Sci. U.S.A.* **114**, 12952–12957 (2017).
30. J. A. Nirody, A. L. Nord, R. M. Berry, Load-dependent adaptation near zero load in the bacterial flagellar motor. *J. R. Soc. Interface* **16**, 20190300 (2019).
31. J. Yuan, K. A. Fahrner, L. Turner, H. C. Berg, Asymmetry in the clockwise and counterclockwise rotation of the bacterial flagellar motor. *Proc. Natl. Acad. Sci. U.S.A.* **107**, 12846–12849 (2010).
32. Y. Chang et al., Molecular mechanism for rotational switching of the bacterial flagellar motor. *Nat. Struct. Mol. Biol.* **27**, 1041–1047 (2020).
33. G. Meacci, G. Lan, Y. Tu, Dynamics of the bacterial flagellar motor: The effects of stator compliance, back steps, temperature, and rotational asymmetry. *Biophys. J.* **100**, 1986–1995 (2011).
34. E. V. Sokurenko, V. Vogel, W. E. Thomas. Catch-bond mechanism of force-enhanced adhesion: Counterintuitive, elusive, but... widespread? *Cell Host Microbe* **4**, 314–323 (2008).
35. W. E. Thomas, V. Vogel, E. Sokurenko, Biophysics of catch bonds. *Annu. Rev. Biophys.* **37**, 399–416 (2008).
36. C. V. Gabel, H. C. Berg, The speed of the flagellar rotary motor of Escherichia coli varies linearly with protonmotive force. *Proc. Natl. Acad. Sci. U.S.A.* **100**, 8748–8751 (2003).
37. E. R. Hosking, C. Vogt, E. P. Bakker, M. D. Manson, The Escherichia coli MotAB proton channel unplugged. *J. Mol. Biol.* **364**, 921–937 (2006).
38. Y. V. Morimoto, Y.-S. Che, T. Minamino, K. Namba, Proton-conductivity assay of plugged and unplugged MotA/B proton channel by cytoplasmic phluorin expressed in Salmonella. *FEBS Lett.* **584**, 1268–1272 (2010).
39. S. Kojima et al., The helix rearrangement in the periplasmic domain of the flagellar stator B subunit activates peptidoglycan binding and ion influx. *Structure* **26**, 590–598.e5 (2018).
40. Y. V. Morimoto, S. Nakamura, N. Kami-ike, K. Namba, T. Minamino, Charged residues in the cytoplasmic loop of MotA are required for stator assembly into the bacterial flagellar motor. *Mol. Microbiol.* **78**, 1117–1129 (2010).
41. S. Kojima, N. Nonoyama, N. Takekawa, H. Fukuoka, M. Homma, Mutations targeting the C-terminal domain of FliG can disrupt motor assembly in the Na+-driven flagella of Vibrio alginolyticus. *J. Mol. Biol.* **414**, 62–74 (2011).
42. B. L. Carroll et al., The flagellar motor of Vibrio alginolyticus undergoes major structural remodeling during rotational switching. *eLife* **9**, e61446 (2020).
43. V. D. Gordon, L. Wang, Bacterial mechanosensing: The force will be with you, always. *J. Cell Sci.* **132**, jcs227694 (2019).
44. R. Chawla, R. Gupta, T. P. Lele, P. P. Lele, A skeptic's guide to bacterial mechanosensing. *J. Mol. Biol.* **432**, 523–533 (2020).
45. Y. F. Dufrêne, A. Persat, Mechanomicrobiology: How bacteria sense and respond to forces. *Nat. Rev. Microbiol.* **18**, 227–240 (2020).
46. B.-J. Laventie, U. Jenal, Surface sensing and adaptation in bacteria. *Annu. Rev. Microbiol.* **74**, 735–760 (2020).
47. G.-L. Ma, H. Chandra, Z.-X. Liang, Taming the flagellar motor of pseudomonads with a nucleotide messenger. *Environ. Microbiol.* **22**, 2496–2513 (2020).
48. C. M. Toutain, N. C. Caizza, M. E. Zegans, G. A. O'Toole, Roles for flagellar stators in biofilm formation by Pseudomonas aeruginosa. *Res. Microbiol.* **158**, 471–477 (2007).
49. I. Hug, S. Deshpande, K. S. Sprecher, T. Pfohl, U. Jenal, Second messenger–mediated tactile response by a bacterial rotary motor. *Science* **358**, 531–534 (2017).
50. A. E. Baker et al., Flagellar stators stimulate c-di-GMP production by Pseudomonas aeruginosa. *J. Bacteriol.* **201**, e00741 (2019).
51. B.-J. Laventie et al., A surface-induced asymmetric program promotes tissue colonization by Pseudomonas aeruginosa. *Cell Host Microbe* **25**, 140–152.e6 (2019).
52. D. C. Wu et al., Reciprocal c-di-GMP signaling: Incomplete flagellum biogenesis triggers c-di-GMP signaling pathways that promote biofilm formation. *PLoS Genet.* **16**, e1008703 (2020).
53. D. M. Hershey, A. Fiebig, S. Crosson. Flagellar perturbations activate adhesion through two distinct pathways in Caulobacter crescentus. *mBio* **12**, e03266-20 (2021).
54. R. N. Perham, D. C. Phillips, G. K. Radda, Self-assembly of biological macromolecules. *Philos. Trans. R. Soc. Lond. B Biol. Sci.* **272**, 123–136 (1975).
55. B. Alberts, The cell as a collection of protein machines: Preparing the next generation of molecular biologists. *Cell* **92**, 291–294 (1998).
56. S. Subramanian, D. B. Kearns, Functional regulators of bacterial flagella. *Annu. Rev. Microbiol.* **73**, 225–246 (2019).
57. H. C. Berg, L. Turner, Torque generated by the flagellar motor of Escherichia coli. *Biophys. J.* **65**, 2201–2216 (1993).
58. X. Chen, H. C. Berg, Torque-speed relationship of the flagellar rotary motor of Escherichia coli. *Biophys. J.* **78**, 1036–1041 (2000).